# CHAPTER 4

# RESULTS AND DISCUSSIONS

This chapter consists of two sections: single-pulse and HRR studies. In single-pulse study, the laser output energy and conversion efficiency were studied with respect to the preionizer-to-main time delay, the storage capacitor voltage, and the storage capacitance. In the second section, laser output power was measured with respect to the HRR frequency, gas flow velocity, and the storage capacitance.

## 4.1 SINGLE-PULSE OPTIMIZATION

It is important to know the single-pulse operating conditions of a TEA $CO_2$ laser before the HRR operation. A normal two-stage spark gap and single-phase H.V. power supply were used in this study and the output energy of the laser pulse was measured by a power/energy meter (Scientech 38-0202 detector and 36-5002 indicator, 20 W or 20 J maximum capability).

### 4.1.1 Laser Beam Characteristics

Fig. 4.1 shows the temporal characteristics of the laser beam, which was measured by a photon drag detector (Rofin-Sinar 7441) and monitored by an oscilloscope (Tektronix TDS 320, 100 MHz, 500 MS/s). The main discharge voltage at position just after the main storage capacitor was also measured by a 1000× attenuation H.V. probe (Iwatsu HV-P30, 30 kVdc, risetime $\lesssim$ 7 ns). The laser pulse begins 650 ns after the laser channel breakdown (as indicated by the arrow). It has a pulse width (FWHM) of about 100 ns and a nitrogen tail of about 3 μs.

The burn patterns of the laser beam on a thermal sensitive paper (fax paper) at 1 m away from the output coupler are shown in Fig. 4.2. Different patterns were observed owing to the optical alignment. The transverse modes of the laser beam are clearly seen. However, when the input energy was increased, high order modes would overlap with the low order modes to give a more uniform laser beam profile.

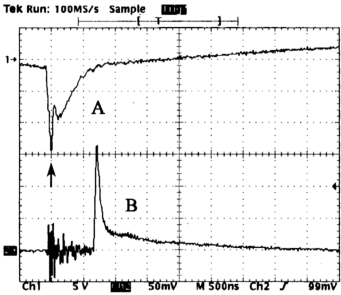


Fig. 4.1: Temporal behaviour of laser beam. $C_{Ms}$ = 40 nF, $C_{Mp}$ = 1.76 nF, $C_{Ps}$ = 4 nF, $C_{Pp}$ = 1.73 nF, and the storage capacitors voltage $V_C$ = 15 kV. A - discharge voltage and B - laser pulse.

Fig. 4.2: Laser burn patterns on thermal sensitive paper. The operating conditions are the same as in Fig. 4.1. The dimensions of the first burn pattern on the left are 0.7 cm × 1 cm.

### 4.1.2 Effects of Time Delay

The time delay between the preionizer and main discharge in this project is defined, as shown in Fig. 4.3, between the first negative peak of the preionizer voltage and the main discharge breakdown, which is the maximum voltage. Note that the first negative peak of the preionizer voltage is not the time when the preionizer breakdown occurs. The preionizer breakdown is at the time around the second peak. This is because the voltage was measured just after the $C_{Ps}$ where is far from the preionizer. Owing to erosion of the preionizer spark electrodes after a number of discharges, the delay in the breakdown of the preionizer was gradually increased, as shown in Fig. 4.4. Therefore, this time delay was often monitored during the HRR TEA $CO_2$ operation in order to ensure that there was sufficient time delay for achieving uniform glow discharge in the laser channel. The dependance of this time delay on the second-stage gap distance of the two-stage discharge spark gap is shown in Fig. 4.5. This figure shows that the time delay also depends on the storage capacitor voltage ($V_C$). The magnitude of the breakdown jitter increases with the second-stage gap distance, as shown by the error bars.

The effects of the time delay on the laser output power is shown in Figs. 4.6, 4.7, and 4.8 for $C_{Ms}$ = 20, 40, and 65 nF. Larger values of preionizer storage and peaking capacitances were used for increasing its ultraviolet intensity (see §4.1.3) for $C_{Ms}$ = 40 and 65 nF. We observed larger error bars in the laser output energy (Fig. 4.8) for $V_C$ = 15.7 kV. In Fig. 4.7, although the storage energy for $C_{Ms}$ = 40 nF and $V_C$ = 23.3 kV (10.86 J) is larger than that in Fig. 4.8 for $C_{Ms}$ = 65 nF and $V_C$ = 15.7 kV (8.01 J), the value of $\sqrt{(LC)}$ is smaller for the former. This may mean that the main discharge duration can affect the output energy fluctuation. The input energy densities for both cases are 136 J/*l*-atm and 100 J/*l*-atm respectively, which are in the normal operating region of a TEA $CO_2$ laser. Further increase in the charging voltage or $V_C$, as shown in Fig. 4.8, caused arcing in the laser discharge. The minimum time delay for stable output

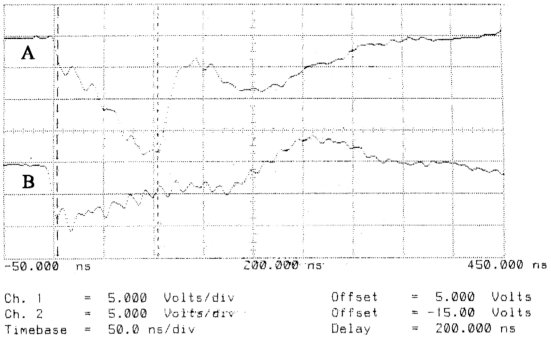


Fig. 4.3: Main (A) and preionizer (B) voltage waveforms. The time delay is defined as shown by the dash lines (Waveforms was taken using a HP54111D, 1 GS/s oscilloscope). $V_C$ = 16 kV.

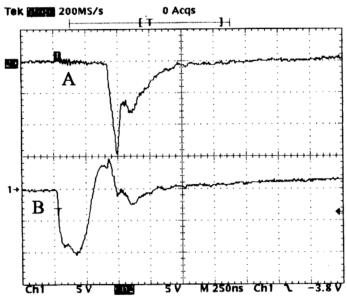


Fig. 4.4: Delayed preionizer breakdown after preionizer gaps become larger after a number of discharges. A - main, B - preionizer. $V_C$ = 15 kV.

energy increases with the $C_{Ms}$ since higher photoelectron densities were needed for larger input energies. However, the minimum time delay reduces when the voltage $V_C$ was increased for a fixed value of $C_{Ms}$. This is because increasing $V_C$ increases the preionizer current and energy, which produces stronger ultraviolet radiation, and hence the photoelectron density (see §3.4) [90]. The main storage energy also increases with $V_C$ but its effect on the output energy fluctuation was smaller than the output energy stabilization by the preionizer when $V_C$ is increased. Note also that both the charging times of the $C_{Pp}$ and the $C_{Mp}$ to their peak voltages (the voltages of breakdowns of the preionizer and main) are decreased when $V_C$ is increased. However, a faster charging time of $C_{Pp}$ gives a higher peak voltage of $C_{Pp}$. This higher peak voltage also gives a higher peak current in the preionizer peaking loop.

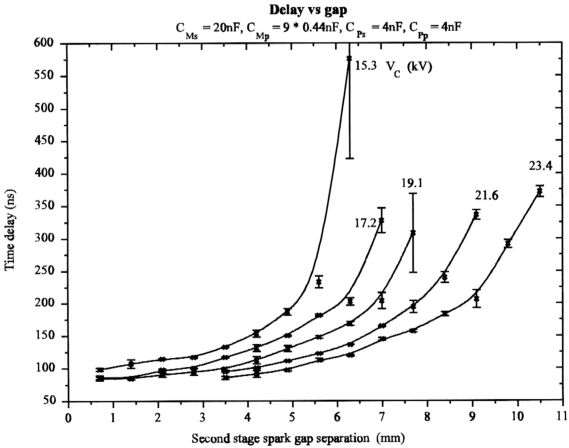


Fig. 4.5: Delay time as a function of second stage gap distance.

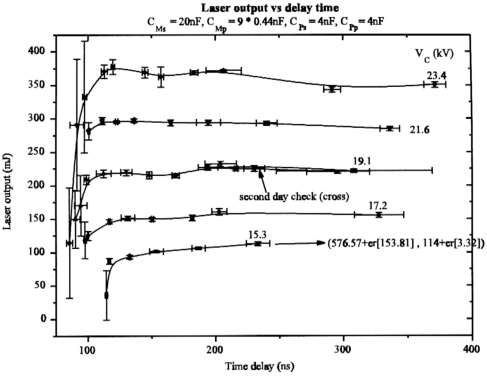


Fig. 4.6: Laser output energy as a function of time delay for $C_{Ms}$ = 20 nF.

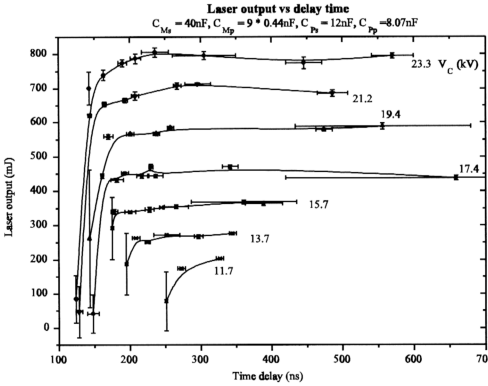


Fig. 4.7: Laser output energy as a function of time delay for $C_{Ms}$ = 40 nF.

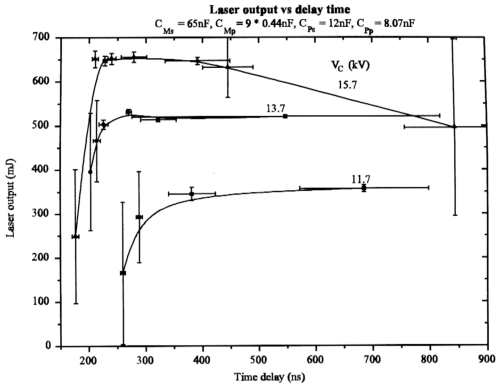


Fig. 4.8: Laser output energy as a function of time delay for $C_{Ms}$ = 65 nF.

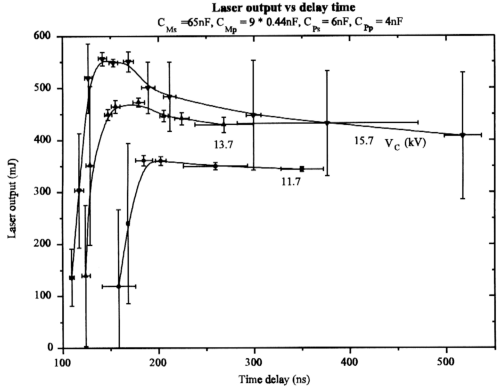


Fig. 4.10: Laser output energy as a function of time delay with smaller $C_{Ps}$ and $C_{Pp}$ if compared to Fig. 4.8.

### 4.1.3 Effect of Preionzer Storage and Main Peaking Capacitances

Fig. 4.9 shows that the effect of the preionizer storage capacitance $C_{Ps}$ on the laser output energy is minimal at $V_C = 23.3$ kV. However, for $C_{Pp} / C_{Ps} > 1$ and $V_C < 15.7$ kV, the preionizer either produced insufficient preionization level or did not break down at all, therefore, the ratio $C_{Pp} / C_{Ps} \leq 1$ must be used.

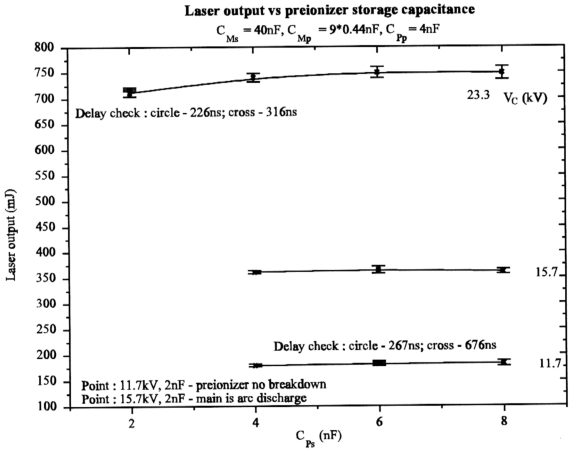


Fig. 4.9: Effect of preionizer storage capacitance on laser output energy.

The $C_{Ps}$ with constant $C_{Pp}$ / $C_{Ps}$ has a significant effect on the laser output energy stability when the main storage capacitance and its voltage are high (main storage energy > 8 J). In Fig. 4.8, for the case of $C_{Ps}$ = 12 nF and $C_{Pp}$ = 8 nF, the laser output energy starts to decrease earlier and the decreasing rate is faster as a function of the time delay. This effect is also shown in Fig. 4.10. For this latter case, since the $\sqrt{(LC)}$ of the preionizer loop was decreased, the time delay also decreased. The output energy fluctuation for the case of smaller $C_{Ps}$ and $C_{Pp}$ also increased when compared to Fig. 4.8, but the maximum output energies decreased for $V_C$ = 13.7 kV and $V_C$ = 15.7 kV.

The effect of the main peaking capacitance $C_{Mp}$ on maximum $C_{Ms}$ for stable laser output energy is shown in table 4.1. The $C_{Mp}$ effect becomes important for $V_C \geq 15.7$ kV and input energy > 7 J. It is noted that the value $\sqrt{LC}$ is also a limiting factor. When $V_C$ = 23.3 kV, the input energy is increased by ~ 3 J. The dependence of $C_{Mp}$ on the laser output energy is not carried out owing to the difficulty of mirrors alignment and changing of $C_{Mp}$.

Table 4.1: The effect of $C_{Mp}$ on the maximum $C_{Ms}$ value for stable output energy.

| $V_C$ (kV) | | 11.7 | 13.7 | 15.7 | 17.4 | 19.4 | 21.2 | 23.3 |
|---|---|---|---|---|---|---|---|---|
| I | $C_{Ms}$ (nF) | 65 | 65 | 65 | 57 | 49 | 49 | 49 |
| | $E_{Ms}$ (J) | 4.45 | 6.1 | 8.01 | 8.63 | 9.22 | 11.01 | 13.3 |
| II | $C_{Ms}$ (nF) | 65 | 65 | 57 | 57 | 49 | 49 | 40 |
| | $E_{Ms}$ (J) | 4.45 | 6.1 | 7.02 | 8.63 | 9.22 | 11.01 | 10.86 |

I -- $C_{Mp} = 9 \times 0.44$ nF

II -- $C_{Mp} = 4 \times 0.44$ nF

Both $C_{Ps}$ = 12 nF, $C_{Pp}$ = 8.07 nF

$C_{Ms}$ is increased by 4 nF each step

### 4.1.4 Output Energies and Efficiencies

The laser output energy and efficiency were measured with respect to the main storage capacitor voltage and its capacitance, as shown in Figs. 4.11 - 4.14. For these results, the time delays were adjusted to the corresponding stable output energy region, as shown in the previous Figs. 4.6 - 4.8 and 4.10. The experiments were performed with fixed main storage capacitance and by varying its voltage. Each data point is an average value of at least five consecutive readings.

In Fig. 4.11, the laser output energy increases almost linearly with $V_C$. The lasing threshold of this laser is about 1 J input energy, as shown by $C_{Ms}$ = 12, 16, and 20 nF. For high $C_{Ms}$ (>40 nF), the laser output energies were limited by the unstable discharge at high input energies loading and/or slow discharge time ($\sqrt{LC}$ ) as mentioned in chapter 2.

Fig. 4.12 shows the laser efficiency as a function of charging voltage. For small storage capacitance ( $C_{Ms} \lesssim 28$ nF), the efficiency increases with $V_C$. It is because there is more energy for discharge excitation of this TEA $CO_2$ laser which in turn overcomes the losses, such as cavity losses, although E/N has been increased. For the case of $C_{Ms} \gtrsim 53$ nF, where there is sufficient energy for creating a population inversion, further increase in $V_C$ will cause E/N to increase which in turn decreases the excitation efficiency, as discussed in Chapter 2 on the dependence of the laser efficiency on the values of E/N.

In order to investigate the effect of $C_{Ms}$ on the laser output energy, the above two graphs were re-plotted, as shown in Figs. 4.13 and 4.14 respectively. The same explanation for Fig. 4.11 is used for Fig. 4.13. However, in Fig. 4.14, efficiencies are increased for all $V_C$ up to $C_{Ms}$ = 28 nF. The highest efficiency is obtained at $C_{Ms}$ = 65 nF and $V_C$ = 11.7 kV, which gives a value of about 10.5%. This is due to the lower E/N value with peak current while there is sufficient input energy for overcoming losses (§2.4). Since the laser pulse output begins in the afterglow regime

(Fig. 4.1), superelastic scattering losses are also effective to reduce population inversion. By maintaining a large current pulse during the lasing action by increasing the $C_{Ms}$ value, it would help to improve the laser efficiency by offsetting the superelastic scattering losses.

Figures 4.15 and 4.16 show another two sets of experimental data with different $C_{Ps}$ and $C_{Pp}$ but both have the same $C_{Pp}$ / $C_{Ps}$ ratio. Figure 4.15 shows that there is a discontinuity of the laser output at $C_{Ms}$ = 40 nF and 41 nF. This may be caused by mirror misalignment. The difference between Figs. 4.15 and 4.16 for maximum $C_{Ms}$ and $V_C$ may be due to the electrode surface cleanliness since Fig. 4.15 was taken with a cleaner electrode surface and new preionizer electrodes just after the system was prepared.

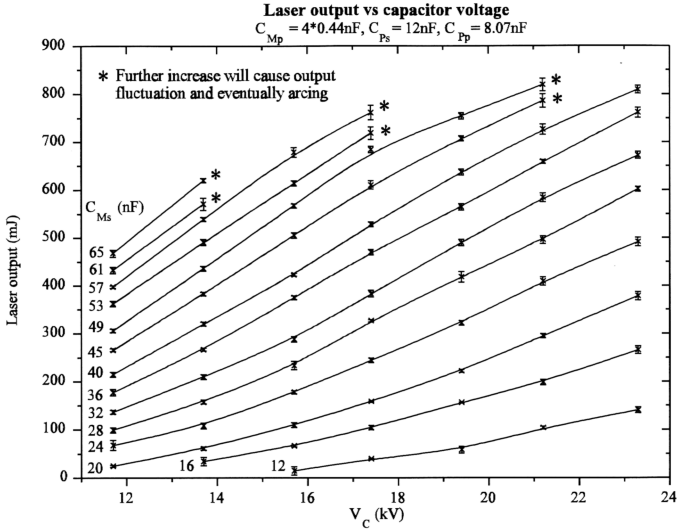


Fig. 4.11: Output energy as a function of storage capacitor voltage.

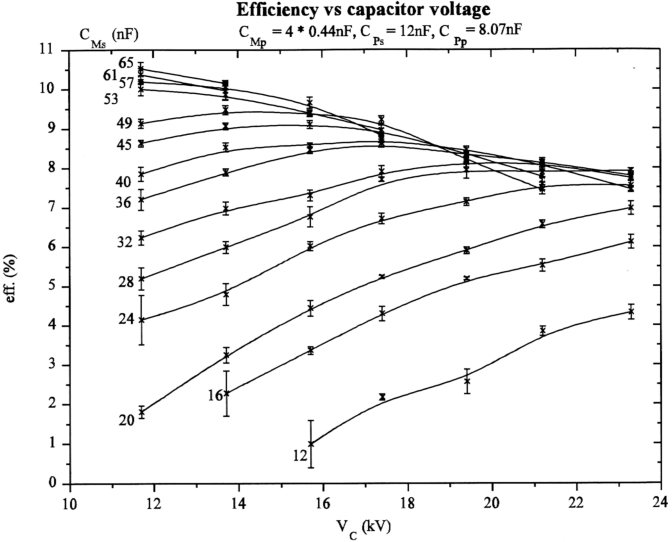


Fig. 4.12: Laser efficiency as a function of storage capacitor voltage.

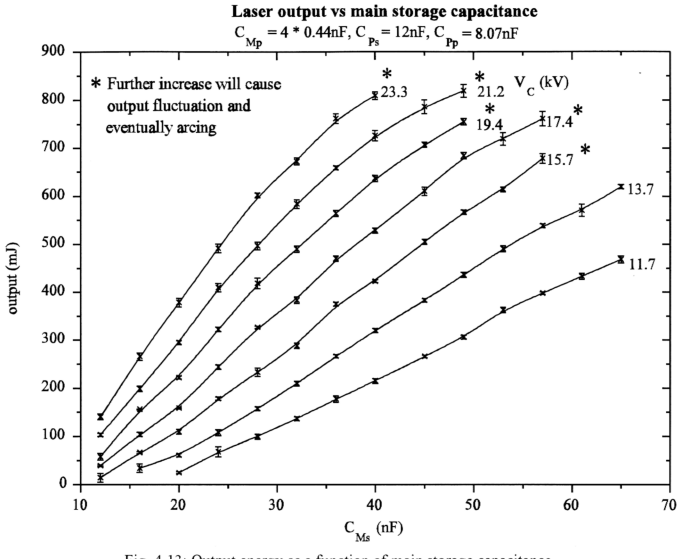


Fig. 4.13: Output energy as a function of main storage capacitance.

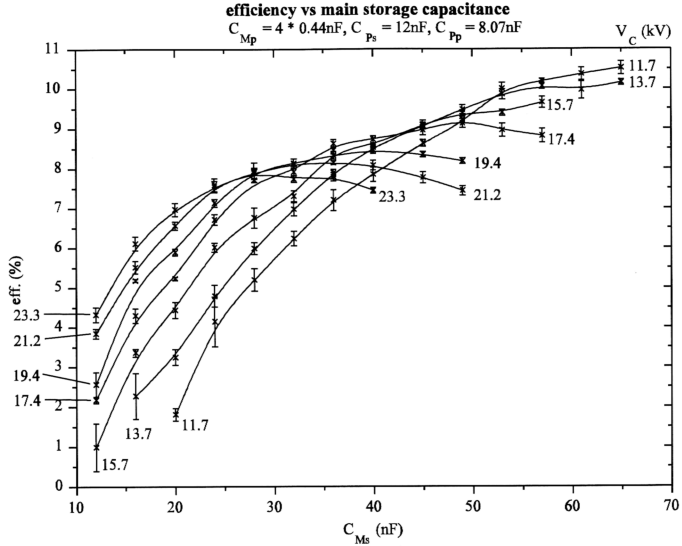


Fig. 4.14: Laser efficiency as a function of main storage capacitance.

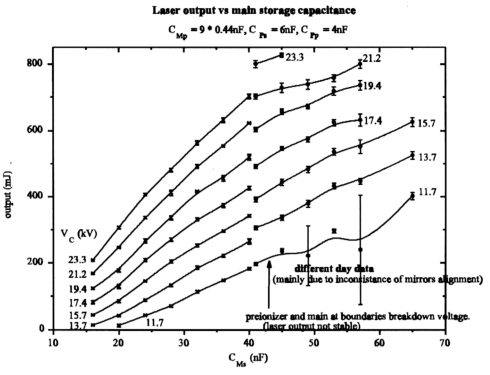


Fig. 4.15: Output energy as a function of main storage capacitance with $C_{Ps}$= 6 nF and $C_{Pp}$= 4nF.

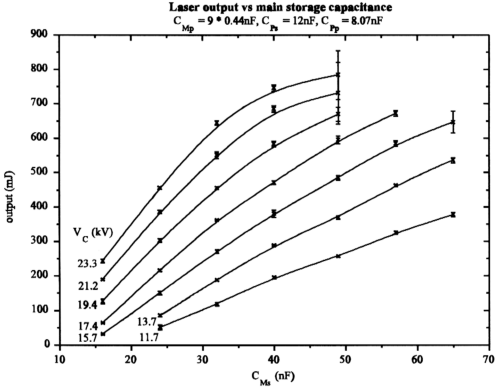


Fig. 4.16: Output energy as a function of main storage capacitance with $C_{Ps}$ =12 nF and $C_{Pp}$ = 8.07 nF.

## 4.2 HRR OPERATION

The following considerations were taken:

(a) Preionizer electrode erosion. In order to reduce this erosion rate, smaller values of $C_{Ps}$ (4 nF) and $C_{Pp}$ (1.73 nF) were used. Operating at 15 kV and at a frequency 300 Hz, the power delivered into the preionizer gap was about 135 W.

(b) Unstable laser output region was avoided. So a value of $C_{Ms} \leq 40$ nF was used.

(c) Time delay ≥250 ns. This condition was checked during HRR operation in order to produce sufficient preionization.

(d) $V_C = 15$ kV. Since the air-blown spark gap insulator was made from perspex, the two-stage discharge spark gap had corona discharge generated by sharp edges and perspex surfaces for $V_C = 17$ kV. Therefore, $V_C$ was limited to 15 kV. Owing to the fluctuation in power supply smoothing capacitor voltage which is during the HRR operation, this 15 kV was taken to be the average value.

The average output power was measured by a water-cooled calorimeter (Scientech 39-0211, smallest range 300 W with smallest readout scale of 5 W). An initial test of the laser maximum frequency was performed with $C_{Mp} = 4 \times 0.44$ nF (this is the value for all HRR operations), $C_{Ms}$ = 20 nF, and gas flow velocity across the laser channel is 22.2 m/s. The maximum frequency was 480 Hz. Above this frequency, arcs developed in the laser discharge. After that, the maximum frequency dropped to around 300 Hz. This was due to the damage of the electrode surface by the arc discharges, which reduce the arc formation time, as described by Sakai et al. [10] (see §2.3.2). By using Eq. 2.6 and a discharge width of ~1.6 cm, the clearing ratio for 480 Hz is ~ 3 while for 300 Hz is ~4.6.

Figure 4.17 shows the laser average output power as a function of HRR frequency with different interelectrode gas flow velocities. The output power is proportional to the frequency

until arcing occurs in the laser discharge. Since the clearing ratio > 1 for all the 3 velocity cases, the output power should show little difference for a given frequency. The slightly lower value of the gas flow velocity of 12.8 m/s may be due to the changes in certain conditions such as decreasing power supply voltage, calorimeter etc.

Figure 4.18 shows the maximum arc-free frequency as a function of the gas-flow velocity. This frequency is decreased with gas flow velocity. Owing to the gas flow measurement limitation, as mentioned in §3.3, lower gas flow velocity was not studied. Since the gas flow uniformity and the gas flow condition (turbulence or laminar) are changed with gas flow velocity, the CR value may be changed. The accuracy of the gas flow velocity measurement in §3.3 is also a factor causing the non linearity relation between maximum arc-free discharge frequency and gas flow velocity. Since the reading of the differential pressure, as generated by the pitot tube, was less than the smallest scale of the differential pressure meter, this may give considerably reading error and the pressure meter system error.

The effect of input energy on maximum arc-free frequency is shown in Fig. 4.19. This frequency is independent on the storage capacitance or input energy. The input energy densities for 20, 30, and 40 nF cases are 28, 42, and 56 J/l-atm, respectively, which are smaller than the normal TEA $CO_2$ laser operating value (~100 J/l-atm). Therefore, this is the diffusion limit region as mentioned in §2.6 (It has to be noted that 1 J/l in Fig. 2.10 corresponds to 1.49 J/l-atm). For this range of energies, the CR value should be closer to the theoretical limit of $\sqrt{3}$. However, The CR values in this experiment are far higher than $\sqrt{3}$. These may be caused by (a) the inaccuracy of the gas flow measurement, (b) the gas flow uniformity between the electrodes, (c) the preionization and main discharge scheme which cannot provide uniform discharge when a small amount of impurity is present in the discharge volume. Figure 2.10 shows that the maximum arc-free frequencies are more sensitive to input energy densities when input energy

density is increased with starting at around 40 J/l (or 60 J/l-atm). The input energy densities of this experiment are below the starting value, so that their effect on maximum arc-free frequency are the same. Operating the laser at input energy densities >60 J/l-atm is needed to observe this effect, but these values are beyond the present system capability at HRR operation.

Fig. 3.19 also shows the data taken using a Scientech 38-0202 calorimeter as a comparison. It seems that the water-cooled calorimeter is out of calibration. Measurements were done for this three $C_{Ms}$ values at 40 Hz: 40 nF/15 W, 30 nF/8.14 W, and 20 nF/3.97 W. The corresponding output energy per pulse are ~375 mJ, ~300 mJ, and ~100 mJ. Therefore, at a frequency of 300 Hz, these give 113 W, 90W, and 30 W respectively.

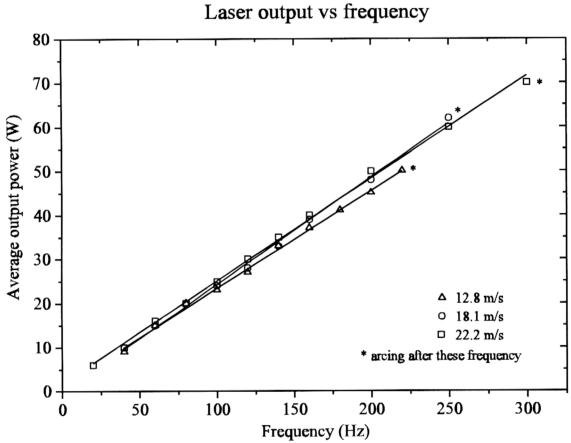


Fig. 4.17: Laser average output power as a function of frequency with different gas flow velocities. $C_{Ms}$ = 40 nF.

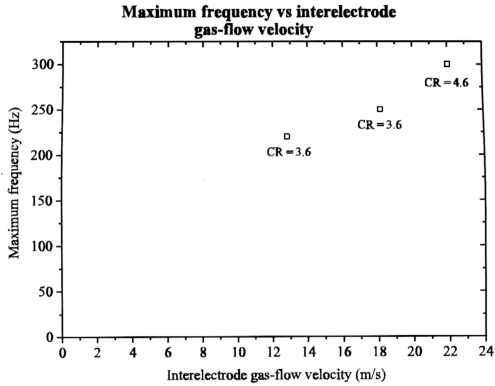


Fig. 4.18: Maximum arc-free frequency as a function of interelectrode gas flow velocity. $C_{Ms}$ = 40 nF.

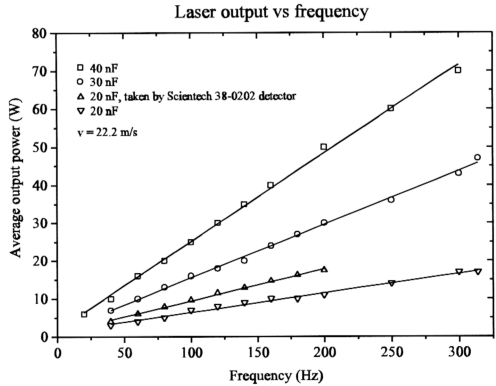


Fig. 4.19: Laser average output power as a function of frequency with different $C_{Ms}$.